PAPER

Check for updates

Deformation of leukaemia cell lines in hyperbolic microchannels: investigating the role of shear and extensional components†

Monica Piergiovanni, [iD] *[a] Valeria Galli,[a] Gregor Holzner,[b] Stavros Stavrakis, [iD] [b] Andrew DeMello [iD] [b] and Gabriele Dubini [iD] [a]

The mechanical properties of cells are of enormous interest in a diverse range of physio and pathological situations of clinical relevance. Unsurprisingly, a variety of microfluidic platforms have been developed in recent years to study the deformability of cells, most commonly employing pure shear or extensional flows, with and without direct contact of the cells with channel walls. Herein, we investigate the effects of shear and extensional flow components on fluid-induced cell deformation by means of three microchannel geometries. In the case of hyperbolic microchannels, cell deformation takes place in a flow with constant extensional rate, under non-zero shear conditions. A sudden expansion at the microchannel terminus allows one to evaluate shape recovery subsequent to deformation. Comparison with other microchannel shapes, that induce either pure shear (straight channel) or pure extensional (cross channel) flows, reveals different deformation modes. Such an analysis is used to confirm the softening and stiffening effects of common treatments, such as cytochalasin D and formalin on cell deformability. In addition to an experimental analysis of leukaemia cell deformability, computational fluid dynamic simulations are used to deconvolve the role of the aforementioned flow components in the cell deformation dynamics. In general terms, the current study can be used as a guide for extracting deformation/recovery dynamics of leukaemia cell lines when exposed to various fluid dynamic conditions.

Introduction

Cells are the basic functional units of the organism and strongly interact with the external environment *via* different stimuli. Traditionally, diverse aspects of cell behaviour, such as signalling pathways, response to chemical and physical cues and genetic and pathogenic induced mutations, have been probed through the use of molecular biomarkers.[1] That said, in recent years the mechanical properties of cells have been recognized as important indicators of cellular health and function. For example, the role of mechanical properties of the whole cell on specific components such as the cytoskeleton, nucleus and membrane[2] have provided valuable insights into the phenotype state, metastatic potential,[3,4] differentiation state,[5] stem cell quality[6] and leukocyte activation.[7] Moreover, mechanical properties such as membrane stiffness,[8] cortical tension[9] and shear modulus[4]

have been proven to be excellent indicators of pathological states for red blood cells (RBCs) including malaria, diabetes,[2] sickle cell disease, spherocytosis[10] and haemolysis. Indeed, the peculiar mechanical properties of RBC membranes have recently been used as a basis to develop new drug-delivery methods[11] and are also responsible for atypical fluid dynamics in fibre-bundle oxygenators at the microscale.[12]

Deformability is a parameter that comprehensively describes the mechanical behaviour of an entire cell and is traditionally measured *via* micropipette aspiration,[8,9] microfluidic optical stretchers[13] and atomic force microscopy.[14,15] With the advent of microfabrication techniques, a variety of microfluidic systems have been used to assess cell deformability at high throughput and without the need for complex and expensive equipment.[2,10] Additionally, microfluidic platforms coupled with high-speed bright field imaging allow the direct and rapid measurement of cell dimension, morphology and deformability.[16–18]

Microfluidic platforms for this purpose can be divided in two main categories depending on the cell deforming mechanism. First, contraction channels, possessing a smaller cross section than the size of cells, provide for confined induced deformation, whilst channels with a wide cross section allow for a fluid-induced deformation without cell-

[a] Laboratory of Biological Structure Mechanics (LaBS), Department of Chemistry, Materials and Chemical Engineering "Giulio Natta", Politecnico di Milano, piazza Leonardo da Vinci, 32 – 20133 Milan, Italy. E-mail: monica.piergiovanni@polimi.it
[b] Institute for Chemical and Bioengineering, ETH Zürich, Vladimir Prelog Weg 1 – 8093 Zürich, Switzerland
† Electronic supplementary information (ESI) available. See DOI: 10.1039/d0lc00166j

channel wall interactions. In the case of contraction channels, measurements of entry time, transit time and transit velocity through the contraction provide indirect information on cell stiffness.[19] However, a major drawback of such contraction systems is the need to process purified cell populations, where there is minimal variation in cellular dimensions. Specifically, cells larger than the channel dimension will lead to channel blockage, dramatically decreasing the throughput, whereas smaller cells will flow through the system without any significant deformation. Additionally, the effects of wall friction and adhesive phenomena in contraction systems are variable and difficult to quantify.

Fluid-induced deformation within microfluidic systems overcomes the aforementioned drawbacks. Such devices can be used to process heterogeneous cellular populations and are not prone to clogging. Accordingly, a variety of microfluidic designs have been used to separate malaria-infected RBCs from healthy RBCs[20] and leukocyte from whole blood.[21,22] Additionally, such systems have been used to good effect in the automated characterization of large populations of cells at ultra-high-throughput.[21,23]

Interestingly, there has been some debate in regard to the specific nature of fluid-induced forces, since recently a distinct effect on cell deformability between shear and extensional forces has been identified.[24] The complex flow environments that occur inside the body (e.g. in vessel bifurcations and in capillary networks) are a result of both shear and extensional phenomena. Since an accurate characterization of cell behaviour is highly desirable, interest has shifted from simple straight channels that provide shear flow[23,25] to the use of more complex shapes, such as cross slot devices[26–28] and hyperbolic contractions[21,28–30] (Fig. 1). In the former, cells are squeezed in a cross-type geometry by

means of opposite flows from two inlets, reaching a stagnation point with maximum strain in the centre, and rapidly exit from one of the two outlets (Fig. 1a). This geometry provides a pure extensional flow, where the cell is pulled and stretched by the fluid. Conversely, a hyperbolic contraction geometry features only one inlet and one outlet and provides for a linear increase in the flow velocity along the channel, resulting in a constant extensional rate that progressively compresses the cells (Fig. 1b). Unlike cross-shaped devices that provide instantaneous information, with cells only being significantly deformed in the centre, the use of hyperbolic geometries allows for the observation of the progressive deformation of cells along the channel length. Specifically, as the channel cross section shrinks, fluid-induced shear stresses increase deformability, with a peak at the end of the hyperbola. Nevertheless, the use of complex flows has typically been performed using cross-shaped devices on red blood cells,[31] mammalian cell lines[28] and pleural effusions.[32,33] Indeed, and to the best of our knowledge, hyperbolic contractions have only been used to assess the deformability of RBCs, which lack the nucleus and thus are much more easily deformed than normal mammalian cells.[24,29,30,34–36]

In the current work, we aim to further characterize hyperbolic geometries by providing an extensive investigation of the deformability properties of leukaemia cells, through a combined experimental and computational campaign. The use of both hyperbolic contractions and cross-shaped geometries enables the investigation of instantaneous and time-dependent deformation dynamics. Additionally, and with a view to disentangling the role of shear and extensional components of the flow-induced deformation, single-phase fluid dynamic simulations are used to complement existing analytical[37] and finite element models (FEM)[32] approaches.

Materials and methods

Microchannel device fabrication

As noted, a hyperbolic shaped channel geometry was used to study deformation under constant extensional rate. Three different contraction widths (w_c) – all larger than the nominal cell diameter, which is approximately 12 μm for all tested cell lines – and two different lengths of the hyperbolic section (L_c) were studied. For all structures, the upstream width (w_u) and height were kept constant. A measure of the induced strain for varying contraction widths is given by the Hencky strain ε_H,[38] i.e.

$$\varepsilon_H = \int_0^t \dot{\varepsilon}_a d_t = \ln\frac{w_u}{w_c} \qquad (1)$$

$$\dot{\varepsilon}_a = \frac{Q}{L_c h}\left(\frac{1}{w_c} - \frac{1}{w_u}\right) \qquad (2)$$

where $\dot{\varepsilon}_a$ is the apparent extensional rate and h is the channel height. Accordingly, the lower the width at contraction (w_c), the higher the strain acting on the flowing cells. At the end
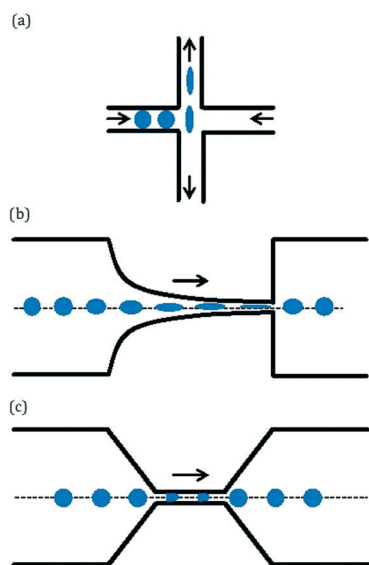

Fig. 1 Representation of the geometries inducing contactless deformation on cells: (a) cross-shaped device, (b) hyperbolic contraction and (c) straight channel.

of the hyperbolic contraction, a sudden expansion was used to investigate cell shape recovery after the release of the fluidic force. The final devices also featured two side channels to deliver a sheath fluid system for cell focusing in the horizontal direction and an array of pillars was added as a filtering unit at each inlet to minimize channel clogging (ESI† Fig. S1). All microfluidic channels had a constant height of 20 μm to facilitate focusing in the vertical direction. Experiments and simulations were also conducted using a cross shaped channel (possessing a square cross-section of 20 μm) and a straight channel (possessing a square cross-section of 20 μm and a length L_c of 300 μm). ESI† Table S1 summarizes critical dimensions of all tested configurations. All the devices were fabricated using standard soft lithography techniques in polydimethylsiloxane.[39] Microfluidic channels were incubated for 10 minutes in a 2% w/w Pluronic F127 (Sigma Aldrich, Buchs, Switzerland) prior to the experiment to prevent cell adhesion to channel surfaces.

Microfluidic devices were mounted on an inverted microscope (Ti-E, Nikon, Zürich, Switzerland) equipped with a white LED light source (SPECTRA X, Lumencor Inc., Beaverton, USA) for bright field imaging (Fig. 2a). A 20× NA 0.45 objective in conjunction with a high-speed camera

(MotionPro Y5, IDT Vision Inc., USA) were used to capture cell deformation events, with sheath fluid and cell stream flow rates regulated with a syringe pump (neMESYS, Cetoni, Germany).

A region of interest (ROI) was defined prior to experiments (Fig. 2b), and high-speed movies were acquired using a minimum shutter speed of 1 μs and a maximum frame rate of 10 000 fps. Analysis of images was accomplished using image-processing algorithms implemented in Python 2.7 and OpenCV 2.4 (details provided in ESI† Note 1). Briefly, the image processing procedure consisted of background subtraction, filtering and contour definition, with parameters such as cell perimeter, cell area and centroid position being extracted. Cell deformation was calculated according to

$$\text{deformation} = 1 - \text{circularity} = 1 - \frac{2\sqrt{\pi A}}{p} \tag{3}$$

where A and p are the area and perimeter of the detected contour, respectively (shown in green in Fig. 2c).

Experimental protocol

When using aqueous media with a dynamic viscosity of approximately 1 mPa s, significant deformation was only observed at linear flow velocities of at least 2 to 3 m s^{-1}. Such high velocities lead to significant motion blur in the collected images. This issue can be addressed through the use of a higher viscosity carrier fluid.[23,40] The addition of methylcellulose (Sigma Aldrich, Switzerland) to PBS creates a shear thinning fluid, with higher density and viscosity than the pure buffer. The high density minimizes cell sedimentation during experiments, whilst the high viscosity enables deformation of cells at significantly lower flow rates. Two buffers with a different methylcellulose concentration were used in the current study.[23] Their characteristics and the respective flow rate employed are summarized in Table 1.

HL60 and Jurkat cell lines (Sigma-Aldrich, Buchs, Switzerland), two widely-used leukaemia cell lines, were cultured in polystyrene flasks using Gibco RPMI 1640 Medium (ThermoFisher Scientific Inc., Waltham, Massachusetts, USA) mixed with 10% (v/v) FBS (Life Technologies, Zug, Switzerland) and 1% (v/v) penicillin–streptomycin (10 000 U mL^{-1}, Life Technologies, Zug, Switzerland). Flasks were stored in an incubator (New Brunswick Galaxy 170S, Eppendorf, Basel, Switzerland) at 37 °C, 5% CO$_2$ and 95% humidity and the medium was refreshed every 2 days. For all experiments cellular
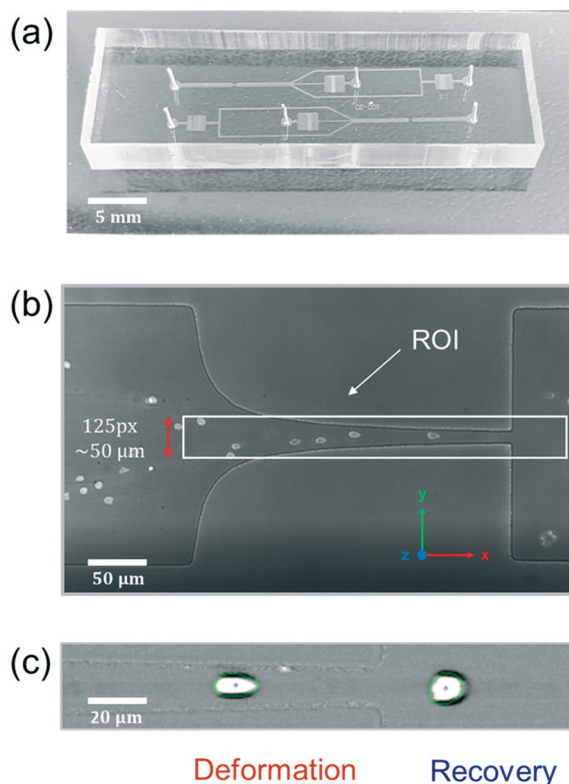

Fig. 2 (a) Image of a microfluidic device integrating a hyperbolic geometry. (b) Snapshot of cells flowing along the hyperbolic microchannel and within a specified region of interest. (c) Distinction between deformed and recovered cells in the contraction and expansion regions, respectively. Here, green contours define the deformed shape as noted in the main text.

Table 1 Range of flow rates for the two buffers used. Values refer to the total flow rate $Q_{\text{tot}} = Q_{\text{sample}} + Q_{\text{sheath}} = 4Q_{\text{sample}}$

	Buffer 0.25	Buffer 0.50
Composition	PBS + MC 0.25% w/v	PBS + MC 0.50% w/v
Density [kg m^{-3}]	1000	1016
Viscosity [Pa s]	0.002 ÷ 0.006	0.004 ÷ 0.015
Q_{tot} [μl min^{-1}]	40, 60, 80, 100	2.4, 4.8, 7.2, 9.6, 14.4

concentrations were maintained at 0.2 million cells per ml. For each experiment, cells were centrifuged (120 rpm for 5 minutes at 24 °C), washed in PBS, filtered through a strainer with a pore size of 40 μm (Corning Inc., New York, USA), centrifuged and re-suspended in the specific buffer. Treatments to modify cell stiffness *via* cell fixation and administration of cytochalasin D were performed as follows. Fixation was performed by addition of a 4% formalin solution for 10 min at room temperature. To prevent the formation of cell aggregates, cells were subsequently washed with PBS supplemented with 10% FBS. After two additional washing steps in PBS the formed pellet was re-suspended in a 0.5% w/v methylcellulose solution. Alternatively, cytochalasin D was dissolved in dimethyl sulfoxide (DMSO) according to a standard protocol.[23] Four different concentrations were used to assess the dose response, *i.e.* 0.01 μM, 0.1 μM, 1 μM and 10 μM. The DMSO concentration was kept constant in all experiments, since it has been previously reported that DMSO alone, and up to 1% final concentration, induces no significant change in deformation.[23]

Computational fluid dynamic simulations

For all the investigated geometries, computational fluid dynamics (CFD) simulations were used to gain additional insight into the fluid dynamics, with particular regard to both shear and extensional rates, *i.e.*

$$\text{shear rate } \dot{\gamma} = \frac{\mathrm{d}v_x}{\mathrm{d}y} \qquad (4)$$

$$\text{extensional rate } \dot{\varepsilon} = \frac{\mathrm{d}v_x}{\mathrm{d}x} \qquad (5)$$

where x is the direction of flow and y the transverse direction (Fig. 2). Rates were calculated along the centreline, where the velocity is maximum and the majority of the cells are located (due to the use of the sheath flow focusing and vertical confinement). All simulations were performed in ANSYS Fluent 19.1 (Ansys Inc., Canonsburg, USA) after importing the geometries from SolidWorks (Dassault Systèmes, Waltham, USA) and building Cartesian meshes with ANSYS Mesher. Geometric symmetry was exploited to save computational time and convergence was always reached within one hour. Single-phase, steady state simulations were performed under laminar flow conditions (ESI† Note 2).

Results and discussion

We initially validated the utility of the hyperbolic contraction as an effective geometry for deformation of HL60 and Jurkat cells, especially in the last narrow region (Fig. 2b) where maximal deformation occurs due to the highest fluid-induced stresses. Plots of deformation as a function of cell area (Fig. 3) show a disperse distribution, with N representing the number of cells in each dataset. Accordingly, and to simplify data visualization, lines enclosing the 50% of the sample are
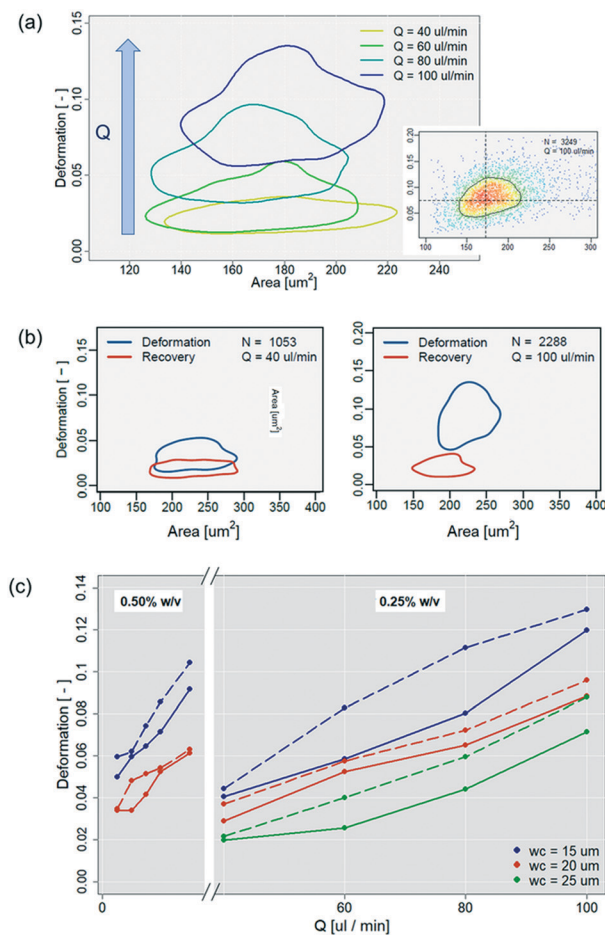

Fig. 3 (a) The increase in deformation as a function of flow rate is shown in plots of deformation *versus* cell area, highlighting the 50% density contour; with the inset showing the complete scatter plot and dashed line displaying the mean deformation and mean area of the sample. (b) The distinction between deformed and recovery populations visualised by means of 50% density contours at the minimum and maximum tested flow rates. (c) Deformation of HL60 cells as a function of volumetric flow rate and hyperbolic channel geometries for the two buffers. Dashed lines highlight long channels ($L_c = 1000$ μm) while solid lines identify short channels ($L_c = 500$ μm).

shown. Unless otherwise stated, the peak of the deformation density distribution (the horizontal dashed line in Fig. 3), that identifies the mean deformation of the sample, was assumed to be representative.

As noted, high-speed brightfield imaging was used to capture and quantify the maximal deformation of cells for a range of flow rates. Fig. 3a confirms that cell deformation increases as a function of volumetric flow rate. At a flow rate of 40 μl min^{-1} (yellow line) the deformation is 0.033 ± 0.002, whilst a flow rate of 100 μl min^{-1} (blue line) induces an almost three-fold higher deformation (0.086 ± 0.004). As volumetric flow rates increase, cells tend to exhibit a larger difference between their deformed and recovered shape; the latter measured in the expansion zone. Moreover, cells that were deformed of values up to 0.1 are still able to recover their original shape (Fig. 3b).

Fig. 3c reports cell deformability for a range of flow rates (up to and including 100 μl min^{-1}) and channel geometries. Channel geometry plays an important role in the cell deformation process, since the use of small contraction widths (blue lines) and longer channel lengths (dashed lines) induce higher shear stresses that deform the contained cells. At the highest tested flow rate of 100 μl min^{-1}, the short channel length with w_c = 15 μm yields a deformation value of 0.12 (solid blue line), compared to 0.07 in the microchannel with w_c = 25 μm (solid green line). Fig. 3c also reports the effect of increasing buffer viscosity on the cell deformability. Using the high viscosity buffer (0.5% methylcellulose w/v), a deformation of 0.06 is obtained at a flow rate of 14.4 μl min^{-1} for the short microchannel with w_c = 20 μm (Fig. 3c left panel, solid red line). Importantly, an identical result can be obtained by increasing the flow rate to 60 μl min^{-1} when using the low viscosity buffer (0.25% methylcellulose w/v) (Fig. 3c right panel, solid red line). Even if no statistical difference in the measured deformability was measured between the two cell lines, the different geometries were able to induce different deformation values, thus showing the capability of the various designs to tune the extensional/shear rates. For HL60 cells, statistically different deformations (p-value < 0.001) can be identified by means of a Mann–Whitney test when comparing channels of different length and contraction width. On the other hand, Jurkat cells show a statistically different deformation only when modifying the contraction width (ESI† Fig. S4).

The use of a hyperbolic channel with a downstream expansion enabled the observation of deformation dynamics along the channel length, as shown in Fig. 4. Both the hyperbolic contraction and the expansion sections were divided in 3 ROIs (bottom panels of Fig. 4), grouping cells that were exposed to similar fluid dynamic solicitation and ensuring a sufficiently high number of processed cells in each region. The mean deformation and standard deviation in each ROI were subsequently extracted. At a constant flow rate, both HL60 and Jurkat cells underwent progressive deformation along the shrinking cross section (Fig. 4a). Moreover, the presence of the abrupt expansion geometry allowed the study of cell recovery after the elimination of the forces induced by the fluid at the contraction (Fig. 4b). In the hyperbolic section, deformation increased almost five-fold for both cell lines, with Jurkat cells demonstrating slightly higher deformation at the end of the contraction channel when compared to HL60 cells. Such an observation agrees well with previous studies, where HL60 have been shown to exhibit enhanced stiffness (due to larger nuclear size) and cortical tension,[15] but also a higher viscosity[41,42] when compared to Jurkat cells. For both cell types, the nucleus is known to be significantly stiffer than the surrounding cytoplasm, which is pervaded by the cytoskeleton.[43] A summary of such literature data for leukaemia cells is provided in ESI† Table S2. Droplets are also reported in the literature as simple models to study cell deformability (ESI† Note 3). However, no reported data can be directly compared to the experiments hereby described, neither in terms of cell viscosity, nor in terms of hydrodynamic force applied to obtain the cell deformation.

Fig. 5 demonstrates the sensitivity of the platform in detecting deformability changes due to softening and stiffening treatments for flow rates up to 14.4 μl min^{-1}. Fixation is a standard technique in cell labelling procedures, inducing proteins cross linking and cell stiffening.
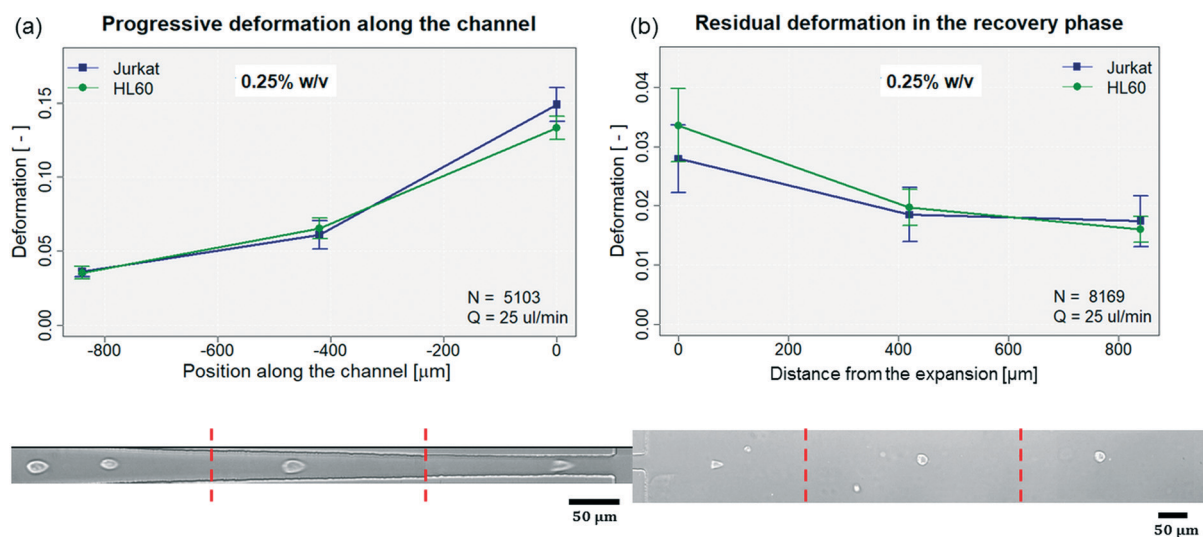

Fig. 4 (a) Deformation as a function of position along the hyperbolic channel and (b) as a function of distance from the expansion for both cell lines at a flow rate of 25 μl min^{-1} and in the low viscosity buffer. Bottom panels indicate the three ROIs used to calculate mean cell deformation. Due to the difference in dimensions between the hyperbolic constriction and the sudden expansion geometries, two objective lenses with different magnifications were used due to high cell velocities (ranging from 0.1 to 1–2 m s^{-1}) approximately three frames for each cell were captured during the deformation process. Using lower flow rates would allow a larger number of frames to be acquired, but at the cost of reduced cell deformation.
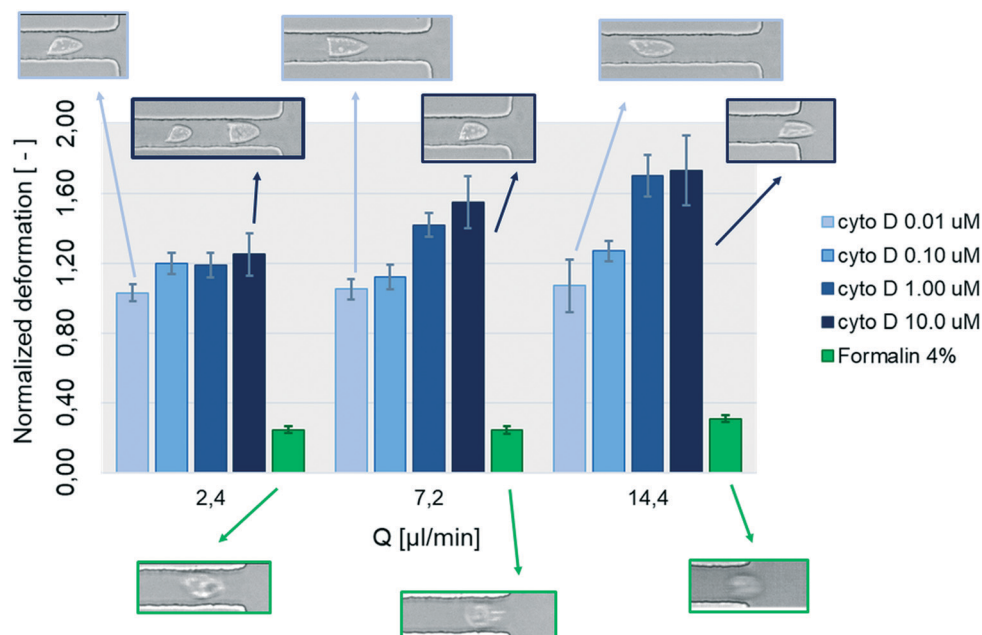
Fig. 5 Normalized deformation (with respect to untreated cells) as a function of cytochalasin D concentration and fixation with 4% formalin at different volumetric flow rates. All data refer to Jurkat cells in the long hyperbolic channel, with L_c = 1000 μm and w_c = 15 μm (the maximum deformation scenario) and in the high viscosity buffer.

Cytochalasin D is a cytoskeleton-altering drug that prevents actin polymerization causing a less organized cytoskeletal structure. Treatment of Jurkat cells with 10 μM cytochalasin D induced an increase in deformation of up to 1.8 times at a flow rate of 14.4 μl min^{-1}, whereas fixation with formalin resulted in normalized deformation values in the range of 0.25 ÷ 0.3. Importantly, such observations are supported by previous studies detailing the effects of cytochalasin D[23,44,45] and formalin[27,45] on leukaemia cells. In the low volumetric flow rate condition (2.4 μl min^{-1}), only modest changes in normalized deformation were observed for Jurkat cells (0.9–1.2) at various drug concentrations, giving rise to only weak
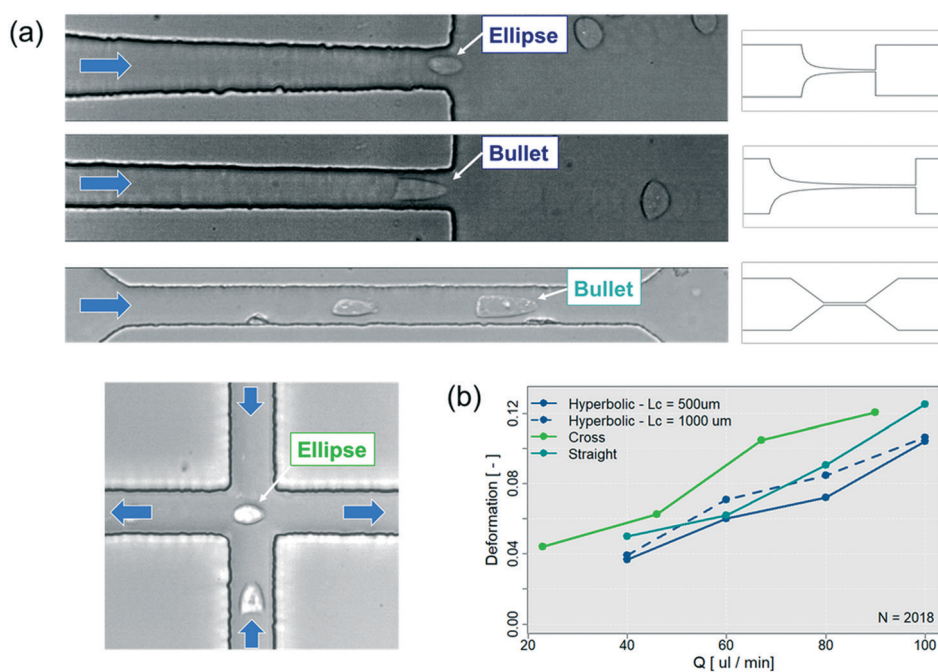

Fig. 6 (a) Images of two modes of deformation shapes occurring in different geometries, with sketching indicating the corresponding geometry. (b) Deformation of Jurkat cells in the different channel geometries with w_c = 20 μm. Dashed line represents the long hyperbolic channel.

changes in the actin cytoskeleton. Conversely, at high volumetric flow rates, cells underwent significant deformation, possibly since the microstructures associated with the actin cytoskeleton are breaking down.

A comparison of deformation shapes in channels of different geometries was also performed. Analysis of deformation in hyperbolic microchannels with the same cross-section of 20 μm, but different lengths, indicated that deformation led to either bullet shaped or elliptical cells (Fig. 6a). The straight microchannel (with the same 20 μm cross section) yielded bullet shaped cells. By comparing cells with the same deformed shape (ellipse), the cross-shaped channel induced a deformation up to 33.3% higher than the short hyperbolic channel (Fig. 6b). Here, the different deformed shape can be justified by the different force that the cross-shaped and hyperbolic geometries impose on the transiting cells. Indeed, it is possible to identify two primary differences, namely the solicitation time (t_s) and the direction of the imposed force. The cross-shaped geometry is designed to create a deforming force that is normal to the cell membrane and one that can be considered to be instantaneous ($t_s < 5$ μs). The hyperbolic channel, on the other hand, imposes a steadily increasing tangential force which occurs over a longer time period (estimated as $t_s > 100$ μs for the short channel and $t_s > 250$ μs for the long channel).

A deeper understanding of the fluid dynamics involved in generating these different deformation shapes was obtained using CFD simulations, which aimed at extracting the extensional and shear contributions in each case and provided a visual representation of the flow characteristics. Fig. 7 summarizes the results from CFD simulations obtained for the short hyperbolic channel at 100 μl min⁻¹. Fig. 7a presents the velocity contour plots from the inlet of the hyperbola (mean value of 0.1 m s⁻¹) to the contraction region, where the velocity increases to a maximum of 10.4 m s⁻¹. A

linear increase in velocity along the centreline implies a constant extensional rate of 21 400 s⁻¹ and increasing shear rate up to the point of maximum contraction, of 5000 s⁻¹ (Fig. 7b and c, with dashed lines marking the start and end of the hyperbolic contraction). It can also be seen that in the sudden expansion part, the difference in buffer viscosities is key to controlling the fluid dynamics with the contour plots in Fig. 7a indicating that a higher viscosity yields a stronger deceleration of the fluid, inducing more rapid cell shape recovery.

On the other hand, for the cross-shaped device a very high extensional rate (320 000 s⁻¹) and zero shear rate are calculated in correspondence with the stagnation point in the centre of the cross (ESI† Fig. S5), whereas the straight channel yields a constant velocity along the cross section, with zero extensional rate and non-zero shear rate (1800 s⁻¹) in Fig. S6.† As concluded from the simulation results, the prevalence of shear forces in the straight and long hyperbolic channels appears to induce a bullet shape cell deformation. In the case of the cross and short hyperbolic channels, the extensional forces play the dominant role in inducing a nearly elliptical shape, as previously observed with other cell lines.[27]

Finally, Fig. 8 shows a comparison of the deformation for both cell lines along with the evaluation of shear and extensional components. In general, a higher contraction width (w_c) leads to lower fluid induced forces and thus reduced deformation, with the cross shaped channel and the straight channel representing the two extreme cases of pure extensional flow and pure shear flow, respectively. The high deformation in the long channel with the smallest tested width ($L_c = 1000$ μm, $w_c = 15$ μm) is likely due to a preponderance of shear effect. Comparing the behaviour of the two cell lines, HL60 cells were found stiffer than Jurkat in all cases (Fig. 8) as also reported in AFM measurements.[15]
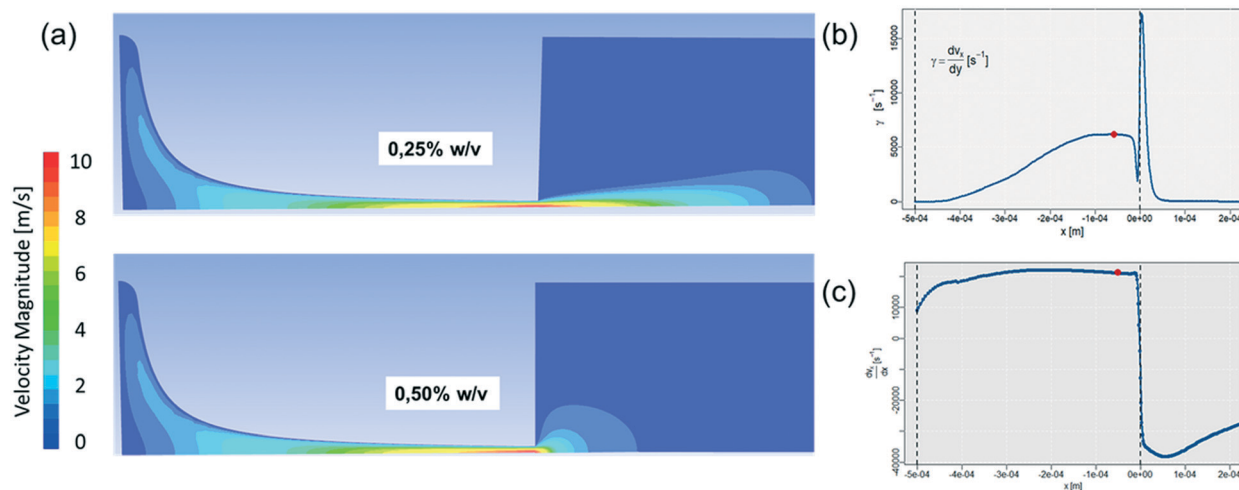

Fig. 7 (a) Velocity contours at mid height ($z = h/2$) in the case of maximum flow rate for the low viscosity and high viscosity buffers. (b) The shear and (c) extensional rate as a function of distance along the centreline with red dots highlighting the mean value in the cross section for each case. Data reported refer to a volumetric flow rate of 100 μl min⁻¹ and short hyperbolic microchannel with $w_c = 15$ μm.
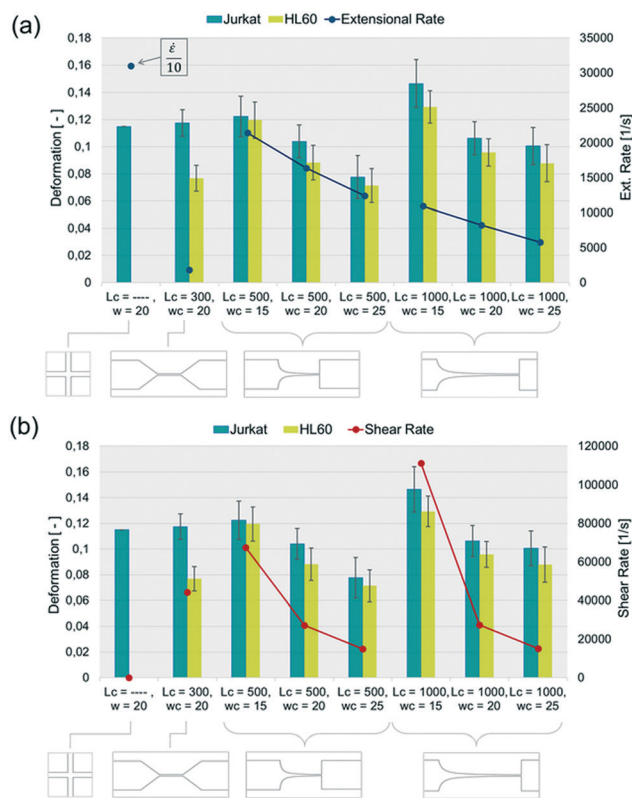
Fig. 8 Measured deformation for all geometries assessed with low viscosity buffer and a total volumetric flow rate of 100 μl min⁻¹ compared to the (a) extensional and (b) shear rates estimated from CFD models.

Conclusions

The present work provides a guide to investigating the fluid-induced deformation of cells, through the accurate assessment of shear and extensional contributions of fluid forces. The use of experimental measurements in different microchannel geometries together with the computational simulations enables the individual evaluation of such contributions and their role in the deformation process. The extensional rate in a hyperbolic channel of fixed length decreases almost linearly with increasing contraction width, inducing a linear decrease in the deformation of both cell lines. By tuning the geometry, it is possible to create completely different balances of shear/extensional contributions at fixed volumetric flow rate, thus inducing different deformation modes and intensities. The use of different geometries, also allows discrimination between quasi-instantaneous fluid dynamic forces (in cross-shaped microchannels) and time-dependent forces (in the straight and hyperbolic channels). The absence of extensional rate is seen to induce a bullet-shaped deformation in both cell lines, while the prevalence of the extensional component yields an elliptical deformation.

The quantification of fluid dynamic variables and the extensive experimental data presented herein provide useful guidelines for the design and operation of microfluidic devices for deformability measurements on a variety of cell types. Taking into account the cell size, and by tuning the microchannel geometry and flow rates, one can accurately set the optimum parameters for deformability measurements. To generate a developed flow in a hyperbolic contraction, which fully quantifies cell deformation, various geometric parameters (such as channel dimensions) can be modified and the flow rate adjusted accordingly, as depicted in Fig. 3. Based on these parameters, the optimum geometry for leukaemia cells was found to be the one with the short channel length width (w_c = 15 μm) at a flow rate of 100 μl min⁻¹, that yields a deformation value of 0.12.

Through the use of the bespoke geometries, it will be possible to investigate the time-dependent deformation dynamics of nucleated cells, paving the way for a thorough analysis of the viscoelastic properties of cells, and engendering a number of different biologically related cell mechanics applications. Indeed, the hyperbolic contraction geometry can be extended to deformability studies of cells that are stiffer than RBCs, such as mechanical phenotyping, isolation of circulating tumour cells in combination with other methods[46,47] or identification of leukocyte activation states.[48,49]

Conflicts of interest

There are no conflicts to declare.

References

1 E. Moeendarbary and A. R. Harris, Cell mechanics: Principles, practices, and prospects, *Wiley Interdiscip. Rev.: Syst. Biol. Med.*, 2014, **6**, 371–388.
2 E. M. Darling and D. Di Carlo, High-Throughput Assessment of Cellular Mechanical Properties, *Annu. Rev. Biomed. Eng.*, 2015, **17**, 35–62.
3 D. Di Carlo, A mechanical biomarker of cell state in medicine, *J. Lab. Autom.*, 2012, **17**, 32–42.
4 S. Suresh, Biomechanics and biophysics of cancer cells, *Acta Biomater.*, 2007, **3**, 413–438.
5 T. Bongiorno, *et al.*, Mechanical stiffness as an improved single-cell indicator of osteoblastic human mesenchymal stem cell differentiation, *J. Biomech.*, 2014, **47**, 2197–2204.
6 R. D. González-Cruz, V. C. Fonseca and E. M. Darling, Cellular mechanical properties reflect the differentiation potential of adipose-derived mesenchymal stem cells, *Proc. Natl. Acad. Sci. U. S. A.*, 2012, **109**, E1523–E1529.
7 M. E. Fay, *et al.*, Cellular softening mediates leukocyte demargination and trafficking, thereby increasing clinical blood counts, *Proc. Natl. Acad. Sci. U. S. A.*, 2016, **113**, 1987–1992.
8 G. W. Schmid-Schönbein, K. L. Sung, H. Tözeren, R. Skalak and S. Chien, Passive mechanical properties of human leukocytes, *Biophys. J.*, 1981, **36**, 243–256.
9 Q. Guo, S. Park and H. Ma, Microfluidic micropipette aspiration for measuring the deformability of single cells, *Lab Chip*, 2012, **12**, 2687–2695.

10 Y. Zheng, J. Nguyen, Y. Wei and Y. Sun, Recent advances in microfluidic techniques for single-cell biophysical characterization, *Lab Chip*, 2013, **13**, 2464–2483.

11 M. Piergiovanni, G. Casagrande, F. Taverna, I. Corridori, M. Frigerio, E. Bianchi, F. Arienti, A. Mazzocchi, G. Dubini and M. L. Costantino, Shear-Induced Encapsulation into Red Blood Cells: A New Microfluidic Approach to Drug Delivery, *Ann. Biomed. Eng.*, 2020, **48**, 236–246.

12 R. Gómez Bardón, A. Passos, M. Piergiovanni, S. Balabani, G. Pennati and G. Dubini, Haematocrit heterogeneity in blood flows past microfluidic models of oxygenating fibre bundles, *Med. Eng. Phys.*, 2019, **73**, 30–38.

13 J. Guck, *et al.*, Optical deformability as an inherent cell marker for testing malignant transformation and metastatic competence, *Biophys. J.*, 2005, **88**, 3689–3698.

14 S. E. Cross, Y. S. Jin, J. Rao and J. K. Gimzewski, Nanomechanical analysis of cells from cancer patients, *Nat. Nanotechnol.*, 2007, **2**, 780–783.

15 M. J. Rosenbluth, W. A. Lam and D. A. Fletcher, Force microscopy of nonadherent cells: a comparison of leukemia cell deformability, *Biophys. J.*, 2006, **90**, 2994–3003.

16 G. Holzner, *et al.*, An optofluidic system with integrated microlens arrays for parallel imaging flow cytometry, *Lab Chip*, 2018, **18**, 3631–3637.

17 S. Stavrakis, G. Holzner, J. Choo and A. DeMello, High-throughput microfluidic imaging flow cytometry, *Curr. Opin. Biotechnol.*, 2019, **55**, 36–43.

18 A. S. Rane, J. Rutkauskaite, A. DeMello and S. Stavrakis, High-Throughput Multi-parametric Imaging Flow Cytometry, *Chem*, 2017, **3**, 588–602.

19 H. W. Hou, *et al.*, Deformability study of breast cancer cells using microfluidics, *Biomed. Microdevices*, 2009, **11**, 557–564.

20 H. W. Hou, *et al.*, Deformability based cell margination - A simple microfluidic design for malaria-infected erythrocyte separation, *Lab Chip*, 2010, **10**, 2605–2613.

21 R. O. Rodrigues, D. Pinho, V. Faustino and R. Lima, A simple microfluidic device for the deformability assessment of blood cells in a continuous flow, *Biomed. Microdevices*, 2015, **17**, 108.

22 S. S. Shevkoplyas, T. Yoshida, L. L. Munn and M. W. Bitensky, Biomimetic autoseparation of leukocytes from whole blood in a microfluidic device, *Anal. Chem.*, 2005, **77**, 933–937.

23 O. Otto, *et al.*, Real-time deformability cytometry: on-the-fly cell mechanical phenotyping, *Nat. Methods*, 2015, **12**, 199–202, 4 p following 202.

24 S. S. Lee, Y. Yim, K. H. Ahn and S. J. Lee, Extensional flow-based assessment of red blood cell deformability using hyperbolic converging microchannel, *Biomed. Microdevices*, 2009, **11**, 1021–1027.

25 Z. Xu, Y. Zheng and X. Wang, *et al.*, Stiffness increase of red blood cells during storage, *Microsyst. Nanoeng.*, 2018, **4**, 17103.

26 Y. B. Bae, *et al.*, Microfluidic assessment of mechanical cell damage by extensional stress, *Lab Chip*, 2016, **16**, 96–103.

27 D. R. Gossett, *et al.*, Hydrodynamic stretching of single cells for large population mechanical phenotyping, *Proc. Natl.*

Acad. Sci. U. S. A., 2012, **109**, 7630–7635.

28 J. S. Dudani, D. R. Gossett, H. T. K. Tse and D. Di Carlo, Pinched-flow hydrodynamic stretching of single-cells, *Lab Chip*, 2013, **13**, 3728–3734.

29 T. Yaginuma, M. S. N. Oliveira, R. Lima, T. Ishikawa and T. Yamaguchi, Human red blood cell behavior under homogeneous extensional flow in a hyperbolic-shaped microchannel, *Biomicrofluidics*, 2013, **7**, 54110.

30 V. Faustino, D. Pinho and T. Yaginuma, *et al.*, Extensional flow-based microfluidic device: deformability assessment of red blood cells in contact with tumor cells, *BioChip J.*, 2014, **8**, 42–47.

31 S. Cha, *et al.*, Cell stretching measurement utilizing viscoelastic particle focusing, *Anal. Chem.*, 2012, **84**, 10471–10477.

32 L. Guillou, *et al.*, Measuring Cell Viscoelastic Properties Using a Microfluidic Extensional Flow Device, *Biophys. J.*, 2016, **111**, 2039–2050.

33 M. Masaeli, D. Gupta and S. O'Byrne, *et al.*, Multiparameter mechanical and morphometric screening of cells, *Sci. Rep.*, 2016, **6**, 37863.

34 R. O. Rodrigues, *et al.*, In vitro blood flow and cell-free layer in hyperbolic microchannels: Visualizations and measurements, *BioChip J.*, 2016, **10**, 9–15.

35 J. S. Bagnall, *et al.*, Deformability of Tumor Cells versus Blood Cells, *Sci. Rep.*, 2015, **5**, 1–11.

36 J. M. Sosa, N. D. Nielsen, S. M. Vignes, T. G. Chen and S. S. Shevkoplyas, The relationship between red blood cell deformability metrics and perfusion of an artificial microvascular network, *Clin. Hemorheol. Microcirc.*, 2014, **57**, 291–305.

37 B. Fregin, *et al.*, High-throughput single-cell rheology in complex samples by dynamic real-time deformability cytometry, *Nat. Commun.*, 2019, **10**, 415.

38 T. J. Ober, S. J. Haward, C. J. Pipe, J. Soulages and G. H. McKinley, Microfluidic extensional rheometry using a hyperbolic contraction geometry, *Rheol. Acta*, 2013, **52**, 529–546.

39 G. Holzner, S. Stavrakis and A. Demello, Elasto-Inertial Focusing of Mammalian Cells and Bacteria Using Low Molecular, Low Viscosity PEO Solutions, *Anal. Chem.*, 2017, **89**, 11653–11663.

40 M. Herbig, A. Mietke, P. Müller and O. Otto, Statistics for real-time deformability cytometry: Clustering, dimensionality reduction, and significance testing, *Biomicrofluidics*, 2018, **12**, 042214.

41 K. Chen, *et al.*, Influence of expressed TRAIL on biophysical properties of the human leukemic cell line Jurkat, *Cell Res.*, 2004, **14**, 161–168.

42 A. E. Ekpenyong, *et al.*, Viscoelastic Properties of Differentiating Blood Cells Are Fate- and Function-Dependent, *PLoS One*, 2012, **7**(9), e45237.

43 N. Caille, O. Thoumine, Y. Tardy and J. J. Meister, Contribution of the nucleus to the mechanical properties of endothelial cells, *J. Biomech.*, 2002, **35**, 177–187.

44 G. Wang, W. Mao, C. Henegar, A. Alexeev and T. Sulchek, Stiffness Dependent Separation of Cells in a Microfluidic

Device, in *ASME 2012 Summer Bioengineering Conference, Parts A and B*, 241 (ASME), 2012, DOI: 10.1115/SBC2012-80095.

45 W. A. Lam, M. J. Rosenbluth and D. A. Fletcher, Chemotherapy exposure increases leukemia cell stiffness, *Blood*, 2007, **109**, 3505–3508.

46 P. Bankó, S. Y. Lee and V. Nagygyörgy, *et al.*, Technologies for circulating tumor cell separation from whole blood, *J. Hematol. Oncol.*, 2019, **12**, 48.

47 N. M. Karabacak, *et al.*, Microfluidic, marker-free isolation of circulating tumor cells from blood samples, *Nat. Protoc.*, 2014, **9**, 694–710.

48 E. Rollo, *et al.*, Label-free identification of activated T lymphocytes through tridimensional microsensors on chip, *Biosens. Bioelectron.*, 2017, **94**, 193–199.

49 E. Bianchi, R. Molteni, R. Pardi and G. Dubini, Microfluidics for in vitro biomimetic shear stress-dependent leukocyte adhesion assays, *J. Biomech.*, 2013, **46**, 276–283.